

Structures and Photophysical Characterization of the Samarium-doped Y₂Mo₃O₁₂ Ceramics

Hyun-Ji Lim

Pusan National University

Min-Seung Kang

Pusan National University

Imjeong H-S. Yang

Pusan National University

Mirang Byeon

Korea Basic Science Institute

Hyun Gyu Kim

Korea Basic Science Institute

Jong Seong Bae

Korea Basic Science Institute

Kyong-Soo Hong (✉ kyongsoo@kbsi.re.kr)

Korea Basic Science Institute <https://orcid.org/0000-0002-9880-7931>

Research Article

Keywords: Y₂Mo₃O₁₂, Sm³⁺, Samarium molybdates, Solid-state reaction, Photophysical properties

Posted Date: March 22nd, 2021

DOI: <https://doi.org/10.21203/rs.3.rs-332064/v1>

License:  This work is licensed under a Creative Commons Attribution 4.0 International License.

[Read Full License](#)

Abstract

Negative thermal expansion materials have been studied in various types of functional materials regardless of their intriguing physical properties. In this study, by introducing Sm³⁺ ions into the Y₂Mo₃O₁₂ lattice, the hygroscopicity is reduced. Y₂Mo₃O₁₂:xSm³⁺ (x = 0.000 ~ 0.300) have been synthesized by using the solid-state reaction method, and their structures have been studied by using thermogravimetric analysis, X-ray diffraction, Raman spectrometry, FT-IR spectroscopy, and nano-SIMS. It is found that the Y₂Mo₃O₁₂:Sm³⁺ is formed in the orthorhombic [Y₂Mo₃O₁₂] phase for lower Sm³⁺ concentrations and samarium molybdates [Sm₂MoO₅] and [Sm₂Mo₃O₁₂] at higher Sm³⁺ concentration samples. Elemental distribution images captured by using a nano-SIMS confirm the existence of [Sm₂MoO₅] and [Sm₂Mo₃O₁₂] phases clearly. Additional phases due to the introducing of Sm³⁺ ions confirm the reduction of atmospheric moisture. Photophysical properties obtained by using absorption and emission spectra reveal that the hygroscopicity-reduced Y₂Mo₃O₁₂:Sm³⁺ can be a possible orange-red-emitting phosphor with the near ultra-violet excitation.

1. Introduction

Molybdates with a general formula A₂Mo₃O₁₂ family, where A is a trivalent cation, are known to be hosts for transition metal ions and lanthanide ions [1-3]. Recently, these materials have attracted lots of attention because of negative thermal expansion (NTE), characterized by chemical flexibility and a phase transition, from monoclinic to orthorhombic, depending on the A³⁺ cation size [4-8]. These NTE materials are microporous and interstitial cation-free frameworks consisting of vertex-linked AO₆ octahedra and MO₄ tetrahedra, where each AO₆ octahedron joins MO₄ tetrahedra sharing oxygen of their corners [1,9]. The correlation between the crystal structure and the thermal expansion in A₂Mo₃O₁₂ is known [10]: A₂Mo₃O₁₂ with larger A³⁺ cations shows more negative overall linear coefficient of thermal expansion than the ones with smaller A³⁺.

However, NTE materials have not been applied widely because of several disadvantages: hygroscopicity, high phase transition temperature, and metastable structure [11,12]. These hygroscopicity and high phase transition temperature in A₂Mo₃O₁₂ family have been studied widely and achieved progresses in practical applications [13-15]: the reduction of hygroscopicity in A₂Mo₃O₁₂ theoretically and experimentally [1,10,11]. Among these molybdates, Y₂Mo₃O₁₂ represents larger NTE because yttrium (Y) has larger ionic radius compared with other trivalent transition metals [9]. In order to understand the NTE mechanisms in Y₂Mo₃O₁₂, several studies have been performed: the relation between AO₆ polyhedral distortion and NTE in orthorhombic Y₂Mo₃O₁₂ [16], and the effect of water species on the phonon modes [11,17]. There are many studies to improve the NTE properties in Y₂Mo₃O₁₂ [18,19], and to characterize various properties of Y₂Mo₃O₁₂ [20-22]. These studies have shown that the hygroscopicity is related to the sizes of cations A, and the reduction of hygroscopicity is achieved by substituting trivalent cations to Y³⁺ sites [10,23]. There is another study about the reduction of hygroscopicity by adding Ce³⁺ ions in

$\text{Y}_2\text{Mo}_3\text{O}_{12}$ [18]. Also, there are many researches about the optical properties in another kind of yttrium molybdate $\text{Y}_2\text{Mo}_4\text{O}_{15}$, as a phosphor material [24-28]. However, it is quite difficult to find the optical studies in $\text{Y}_2\text{Mo}_3\text{O}_{12}$ material [29]. Hence, we start this research to expand the previous results to another rare-earth (RE) ion Sm^{3+} ; i.e. reducing the hygroscopicity and studying the optical properties of $\text{Y}_2\text{Mo}_3\text{O}_{12}$.

RE-activated phosphors have been actively studied for the application in light-emitting diodes because of their chemical stability and relatively simple preparation conditions. Recently we have reported on the structures and optical properties of RE-doped apatites $\text{Ca}_5(\text{PO}_4)_3\text{Cl}$ [30,31] and phosphates [32]. Trivalent samarium (Sm^{3+}) is applied as an activator for lots of phosphors that have red-orange emission arising from its $^4\text{G}_{5/2} \rightarrow ^6\text{H}_J$ ($J = 5/2, 7/2, \text{ and } 9/2$) transitions. Sm^{3+} also determines the photophysical properties of phosphors such as their lifetimes and efficiencies operating under the near ultra-violet (NUV) excitation [33-35]. As a continuation of our work on the optical properties in Sm^{3+} -doped inorganic materials, we investigate the photophysical properties of $\text{Y}_2\text{Mo}_3\text{O}_{12}$.

In this work, we prepare Sm^{3+} -doped $\text{Y}_2\text{Mo}_3\text{O}_{12}$ by using the solid-state reaction method in order to characterize the structures and photophysical properties. First, we report the synthesis procedures. We characterize the structures by using a thermogravimetric analyzer (TGA), an X-ray diffractometer (XRD), a Raman spectrometer, a Fourier-transform infrared (FT-IR) spectrometer, and an X-ray photoelectron spectrometer (XPS). Then we observe the morphology by using a scanning electron microscope (SEM). Also we take elemental distribution images by using a high-resolution secondary ion mass spectrometer (nano-SIMS). Finally, we investigate photophysical properties of the $\text{Y}_2\text{Mo}_3\text{O}_{12}:\text{xSm}^{3+}$ samples by taking absorption, excitation, and emission spectra at room temperature. We show that the hygroscopicity-reduced $\text{Y}_2\text{Mo}_3\text{O}_{12}:\text{Sm}^{3+}$ samples are orange-red-emitting phosphors with the NUV excitation.

2. Experimental Details

$\text{Y}_2\text{Mo}_3\text{O}_{12}:\text{xSm}^{3+}$ powders are prepared by using the solid-state reaction method. The starting materials are yttrium oxide (Y_2O_3 , Kanto Chemical Co. 99.99 %) and molybdenum oxide (MoO_3 , Junsei Chemical Co. 99.5 %). Samarium oxide (Sm_2O_3 , Samchun Chemical Co. 99.9 %) is used as an activator. All reagents are used without further purifications. We vary the amount of dopants while keeping the ratio of Y_2O_3 to MoO_3 as 1:3. The amount of dopant Sm_2O_3 is varied from 0.000 mol (pure) to 0.300 mol. All the reagents are weighed stoichiometrically and thoroughly mixed with a ball mill for 24 h in ethanol and fully dried in an oven at 80 °C overnight. The dried materials are heated in an alumina crucible at 300 °C for 3 h in an electric furnace. The cooled materials are grinded thoroughly and sintered at 700 °C for 12 h in an electric furnace.

The structures of the synthesized powders are investigated by using an XRD (Philips X'PertPro) with Cu-K α radiation ($\lambda = 0.15406$ nm) and with a 0.02° step and a scanning rate of 2°/min in diffraction angle for the scan range of 10° ~ 70°. The XRD is operated at a generating power of 1.2 kW at 30 mA current and

40 kV voltage. The obtained XRD patterns are analyzed by using the JADE and compared with the data from the Joint Committee on Powder Diffraction Standards (JCPDS) for identification of the obtained phases. The morphology is observed by using a SEM (Hitachi SU-70) with an accelerating voltage of 15 kV. TGA (TA Q600) study is carried in the temperature range of 20 ~ 500 °C with heating and cooling rates of 10 °C/min.

The elemental distribution is analyzed qualitatively by using a nano-SIMS (Cameca NS50). Nano-SIMS images are obtained by using a cesium primary ion beam with a diameter 100 nm, an impact energy 16 keV, and a beam current 0.4 pA. The raster size is 20 mm x 20 mm in all images with 256 pixels x 256 pixels for generating qualitative secondary ion images with 30 ms/pixel accumulation time. Samples are simultaneously imaged by taking the secondary ions that are detected by an electron multiplier.

The chemical behavior and the molecular bonding structure are characterized by using a FR-IR (Bruker, Vertex80v) in the range of 4,000 ~ 400 cm^{-1} . All IR spectra are collected with 256 scans and a spectral resolution of 4 cm^{-1} . Raman spectra are measured by using a Raman spectrometer (NanoBase XperRam200) in the range of 0 ~ 3000 cm^{-1} with a laser power of 3 mW ($\lambda = 532 \text{ nm}$) and 128 scans with 0.5 ms accumulation time. The valence states of the elements are studied by using an XPS (Thermo Fisher K-Alpha⁺) with Al Ka ($h\nu = 1486.6 \text{ eV}$) radiation. The XPS is operated at an accelerating voltage of 12 kV with energy 72 W. The measured area is an oval shape with short diameter of 400 μm , and energy step sizes are 1 eV and 0.1 eV for wide and narrow scans, respectively.

The synthesized powder is pressed into pellets with potassium bromide (KBr, Pike Tech. IR Grade) for the optical measurements. Absorption spectra are obtained by using an UV-Vis spectrometer (Agilent Cary 300) with 0.2 nm step and 1 s averaging time. Emission spectra are taken with a steady-state fluorescence system with a 1000 W Xe-lamp. The excitation light from a Xe-lamp (Muller Elektronik-Optik LAX-1000), selected by using a 320 mm focal length monochromator (Dongwoo DM320i), is focused onto the sample. Fluorescence from the sample is collimated and refocused into the emission monochromator (Dongwoo DM320i) with a 320 mm focal length. The collimated emission is detected by using a photomultiplier tube (PMT, Hamamatsu R955) after passing the cut-off filter (Edmund OG 515) and data are accumulated with a computer. All spectra are taken at room temperature.

3. Results And Discussion

Figure 1(a) shows XRD patterns of some of the $\text{Y}_2\text{Mo}_3\text{O}_{12}:x\text{Sm}^{3+}$ powders with concentrations of 0.300, 0.100, 0.010, and 0.000 mol, from top to bottom, and Fig. 1(b) shows the patterns of $[\text{Y}_2\text{Mo}_3\text{O}_{12}]$, $[\text{Sm}_2\text{MoO}_5]$, and $[\text{Sm}_2\text{Mo}_3\text{O}_{12}]$ phases from JCPDS Nos. 28-1451, 31-1214, and 25-0748, respectively. For lower Sm^{3+} concentrations, the observed XRD patterns follow the reference $[\text{Y}_2\text{Mo}_3\text{O}_{12}]$ phase clearly. As we increase the amount of doped Sm^{3+} ions, however, the XRD patterns of $x \geq 0.100$ are distinctively different from those of $x \leq 0.100$. These observations suggest that a phase transition occurs around $x = 0.100$. For higher Sm^{3+} concentrations, new phases samarium molybdates $[\text{Sm}_2\text{MoO}_5]$ and $[\text{Sm}_2\text{Mo}_3\text{O}_{12}]$

are observed along with $[Y_2Mo_3O_{12}]$ phase. The decrease of the peak intensities of $[Y_2Mo_3O_{12}]$ phase with an increase of Sm^{3+} amount means that the crystal structure depends on the doped ion concentrations.

In order to show that these phases are related to the hygroscopicity, we take TGA data. Figure 1(c) shows the weight variations of the samples according to the temperature. A gradual decrease of weight corresponding to the release of adsorbed water and/or crystal water with increasing temperature is observed, which means the reduction of hygroscopicity. In other words, the newly obtained phases look responsible for the reduction of hygroscopicity of the synthesized powders.

For the morphology of the microstructure of the $Y_2Mo_3O_{12}:xSm^{3+}$ powders, SEM images are recorded and represented in Fig. 2 with concentrations of (a) 0.000, (b) 0.005, (c) 0.050, and (d) 0.150 mol, respectively. All images show aggregated grains, and powders have various shapes with a few tens of mm sizes regardless of the doped amount. As mentioned in Experimental Section, we have applied a solid-state reaction method for the sample preparation procedures. Thus, we have powders of aggregated particles caused by the high-temperature sintering process. All the powder samples are found to form similar shapes via SEM images. The morphology of the obtained $Y_2Mo_3O_{12}:xSm^{3+}$ powders do not show any significant phase variations related to the hygroscopicity with the Sm^{3+} concentration.

Nano-SIMS is utilized in elemental analysis, with high spatial resolution, by tracing a small amount of elements and isotopes. With high lateral resolution and sensitivity, the possibility of imaging components based on the elemental and isotopic compositions of atomic and molecular ion fragments can be offered by using a nano-SIMS. The obtained information through nano-SIMS complements other analytical results obtained by using other types of SIMS experiments [36]. Also we can compare elemental distributions clearly at a fixed position of the sample because nano-SIMS can record five atomic mass images simultaneously with a high-resolution of 50 nm. Thus, we have applied this equipment to studying phosphors and reported the element compositional analysis results in phosphor material [37]. In this study, we apply nano-SIMS to our samples rather than energy-dispersive spectrometer (EDS).

We take the elemental acquisition images of oxygen, yttrium, molybdenum, and samarium in the $Y_2Mo_3O_{12}:xSm^{3+}$ samples and represent them in Fig. 3(a) ~ (d), respectively. Sm^{3+} concentrations are 0.000, 0.005, 0.050, and 0.200 mol, respectively, from top to bottom, in each element. These images are taken at high vacuum with ion beam etching the surface of the samples and the scale bar shown in each image has different scales depending on the element. We observe that elements are distributed throughout the samples, although the obtained images provide only qualitative information. Sm^{3+} is observed even in a lower amount-doped sample. At first, when we prepare the samples, we think that Sm^{3+} ions are substituted into Y^{3+} sites through the sintering procedure as in Ref. [18] and in $Y_2Mo_4O_{15}$ case [24-28] because the ionic radii of these are quite close: 104 pm for Y^{3+} and 109.8 pm for Sm^{3+} [38]. However, samarium ions are observed at the molybdenum positions rather than yttrium positions, at higher Sm^{3+} concentrations. As mentioned in XRD pattern results, we observe that there are newly formed

samarium molybdates such as $[\text{Sm}_2\text{MoO}_5]$ and $[\text{Sm}_2\text{Mo}_3\text{O}_{12}]$ in higher concentration powders. Thus, the images obtained by using a nano-SIMS strongly support the discussion of new phases in XRD patterns for the higher Sm^{3+} concentration samples.

For the structural aspect, we take the Raman and the FT-IR spectra of the samples and represent them in Fig. 4. Figure 4(a) shows the Raman spectra of the $\text{Y}_2\text{Mo}_3\text{O}_{12}:x\text{Sm}^{3+}$ samples with Sm^{3+} concentrations 0.300, 0.150, 0.050, and 0.005 mol, respectively, from top to bottom. All the Raman modes are observed nearly at the same positions regardless of the doped amount. The spectral shapes are distinctively different for $x \geq 0.100$ and $x \leq 0.100$ similar to the XRD patterns, which confirms the phase variations with the Sm^{3+} ion concentrations clearly. The modes below 150 cm^{-1} are identified as translational and librational vibrations of the polyhedra YO_6 and MoO_4 [9,10]. The modes in the region $300 \sim 400 \text{ cm}^{-1}$ are bending vibrations of the MoO_4 tetrahedra [10,11]. The modes around 476 cm^{-1} are not identified. The ones in $700 \sim 900 \text{ cm}^{-1}$ and $900 \sim 1,000 \text{ cm}^{-1}$ are asymmetric stretching and internal stretching vibrations of the MoO_4 tetrahedra, respectively [10,11]. The modes around 48 and 97 cm^{-1} become stronger gradually with the doped Sm^{3+} amount, which indicates that translational and librational motions related to doped-REs make a significant contribution to the $\text{Y}_2\text{Mo}_3\text{O}_{12}$ structure. The strong modes around 1100 cm^{-1} which appear in samples with higher concentrations are emission bands due to the transition ${}^4\text{G}_{5/2} \rightarrow {}^6\text{H}_{5/2}$, and this will be discussed later in the emission spectra part.

Figure 4(b) represents the FT-IR spectra of the $\text{Y}_2\text{Mo}_3\text{O}_{12}:x\text{Sm}^{3+}$ with Sm^{3+} concentrations 0.300, 0.100, 0.010, and 0.000 mol, respectively, from top to bottom. The effects caused by atmospheric moisture and carbon dioxide, which are assumed to have been absorbed from air during sample preparation procedures, are removed from each measurement through background subtraction. Clearly we observe the phase variations according to the doped Sm^{3+} amount as in Raman spectra. We represent the regions $3,800 \sim 3,000 \text{ cm}^{-1}$ and $1,800 \sim 400 \text{ cm}^{-1}$ because we are interested in the hygroscopicity of $\text{Y}_2\text{Mo}_3\text{O}_{12}$ and the vibrations of polyhedra MoO_4 and YO_4 . The broad bands in the range $3,700 \sim 3,100 \text{ cm}^{-1}$ are the O-H stretching vibrations depending on the environment. The sharp bands in the range $1,750 \sim 1,530 \text{ cm}^{-1}$ are H_2O bending/O-H bond [39]. Weak intensity bands around $1,460 \text{ cm}^{-1}$ and $1,400 \text{ cm}^{-1}$ are C-OH and O-H bond, respectively. We use only oxides in the synthesis procedure, thus the C-OH is originated from the atmospheric carbon dioxide. The intensities of O-H bonds are comparable to usual materials. Thus, the atmospheric moistures do not affect the prepared samples a lot regardless of the hygroscopicity. The observed peak positions below $1,000 \text{ cm}^{-1}$ region remain almost the same with the doped Sm^{3+} amount as in Raman case. The broad band around $1,000 \sim 700 \text{ cm}^{-1}$ correspond to the vibrations of polyhedra MoO_4 and YO_6 [9-11]. The bands at about 867 cm^{-1} and 936 cm^{-1} (represented by blue vertical dotted lines) correspond to symmetric and asymmetric stretching vibrations of the MoO_4 tetrahedra, respectively [11,18]. These show clear peak position shifts and their relative intensities, respectively, with the doped amount, which means that the influences of atmospheric moisture on the stretching vibrations of the MoO_4 tetrahedra become weaker [11]. As mentioned earlier, we can think that these shifts are related to

the phase variations of the materials with the Sm^{3+} amounts. The small peaks around $600 \sim 400 \text{ cm}^{-1}$ are correspond to the vibrations of polyhedra MoO_4 and YO_6 [2].

From the Raman and the FT-IR spectra shown in Fig. 4, we observe the structural variations as in XRD patterns with the doped Sm^{3+} concentrations. At room temperature $\text{Y}_2\text{Mo}_3\text{O}_{12}$ forms in orthorhombic structure with a space group Pba2 and undergoes a phase transition, ferroelectric-ferroelastic to paraelectric-paraelastic, at higher temperature [40]. Although we have synthesized the $\text{Y}_2\text{Mo}_3\text{O}_{12}$ samples at higher temperature, we have taken the data at room temperature. Thus, we need more study about $\text{Y}_2\text{Mo}_3\text{O}_{12}$ samples whether the reduction of hygroscopicity is directly related to the new phases appeared at higher concentrations.

To see the chemical states of the elements in the prepared powders, we take XPS spectra. Figure 5 represents the wide scan XPS spectra of the $\text{Y}_2\text{Mo}_3\text{O}_{12}:x\text{Sm}^{3+}$ samples with concentrations of 0.300, 0.150, 0.050, and 0.000 mol, respectively, from top to bottom. In XPS spectra, the position on the kinetic energy scale means the difference between the photon excitation energy, and the spectrometer work function corresponds to a binding energy of 0 eV with reference to the Fermi level [41]. All the peak positions are calibrated with respect to carbon 1s at 284.6 eV. Peaks of elements such as Y, Mo, O, and Sm including KLL (oxygen Auger peak) are clearly identified [41]. Other small peaks such as Y 4p/O 2s around 23~24 eV, Mo 4p around 36 eV, Mo 4s around 63 eV, and Mo 3s around 506 eV are not designated in the figure for clarity, even though they are identified. The starting oxides are burned in the atmosphere during sintering process, which means that some of the oxygen atoms from the starting materials are used during the sintering process inside of the furnace. Also, we take XPS spectra in high vacuum without etching the samples. Hence, the observed carbon peaks are from atmospheric carbon dioxide attached to the sample powders during the pre-treatment procedure for the measurements.

To see the effect of Sm^{3+} introducing, we take the narrow scan XPS spectra of the $\text{Y}_2\text{Mo}_3\text{O}_{12}:x\text{Sm}^{3+}$ samples and represent them in Fig. 6. Figure 6(a) ~ (d) shows the spectra of Y 3d orbitals, Mo 3d orbitals, O 1s orbitals, and Sm 3d orbitals, respectively. The dopant concentrations are the same as those in Figure 5 from top to bottom, except for the samarium shown in (d). After introducing Sm^{3+} , the spin-orbit splitting of Y 3d and Mo 3d are 2.0 eV and 3.2 eV, respectively, and these remain unchanged. However, the binding energies of Y $3d_{5/2}$ and Mo $3d_{5/2}$ decrease from 158.0 eV to 157.8 eV and from 232.6 eV to 232.3 eV, respectively. The differences are 0.2 eV and 0.3 eV, respectively. For oxygen, the binding energy shift is 0.2 eV after the Sm^{3+} introducing and the orbital feature looks symmetric. That is, binding energy shifts are quite small even though Sm^{3+} ions are introduced. The differences are the same regardless of the concentration variations. Compared with Ce^{3+} -doped $\text{Y}_2\text{Mo}_3\text{O}_{12}$ in Ref. [18], where Ce^{3+} ions are substituted into the Y^{3+} sites, we have new samarium molybdate phases [Sm_2MoO_5] and [$\text{Sm}_2\text{Mo}_3\text{O}_{12}$] at higher Sm^{3+} concentration samples. These newly-formed materials seem to cause the reduction of the hygroscopicity in the host material, $\text{Y}_2\text{Mo}_3\text{O}_{12}$. Also, Sm^{3+} ions are clearly observed in the samples as shown in Fig. 6(d) even though the doped amounts are very small. The photoelectron lines of the

observed elements Y, Mo, O, and Sm in Figs. 5 and 6 are schematically summarized in Fig. 6(e). The values of the line positions reflect the energies of the elemental peaks observed.

For optical properties, we observe quite similar features in the UV-visible absorption spectra and represent absorption spectra of the $Y_2Mo_3O_{12}:xSm^{3+}$ samples in Figure 7 with the dopant concentrations 0.200, 0.150, and 0.100 mol, from top to bottom. A strong absorption band in the NUV region, corresponding to the ${}^6H_{5/2} \rightarrow {}^4F_{7/2}$ transition from doped Sm^{3+} , is observed around 405 nm. Other identified absorption bands are associated with electronic transitions such as ${}^6H_{5/2} \rightarrow ({}^6P, {}^4P)_{5/2}$ around 420 nm, ${}^6H_{5/2} \rightarrow {}^4G_{9/2}$ around 439 nm, ${}^6H_{5/2} \rightarrow {}^4I_{15/2}$ around 452 nm, ${}^6H_{5/2} \rightarrow {}^4I_{13/2}$ around 464 nm, ${}^6H_{5/2} \rightarrow {}^4I_{11/2}$ around 482 nm, and ${}^6H_{5/2} \rightarrow {}^4I_{9/2}$ around 491 nm [32]. From these bands, we observe that the luminescent features are based on the direct transitions from the ground state ${}^6H_{5/2}$ to the excited states of Sm^{3+} [32].

Figure 8(a) represents the emission spectra taken by excitation of ${}^6H_{5/2} \rightarrow {}^4F_{7/2}$ transition at 405 nm in the $Y_2Mo_3O_{12}:xSm^{3+}$ samples. We show the samples of Sm^{3+} concentrations 0.100, 0.050, and 0.010 mol for clarity. The identified emission bands are ${}^4G_{5/2} \rightarrow {}^6H_{5/2}$ around 566 nm, ${}^4G_{5/2} \rightarrow {}^6H_{7/2}$ around 603 nm, and ${}^4G_{5/2} \rightarrow {}^6H_{9/2}$ around 649 nm, showing the spectral features of the intra 4f-4f transitions of Sm^{3+} . Each band consists of several weak intensity peaks due to the splitting of the ${}^4G_{5/2}$ state arising from the Stark effect [42], which makes the spectral shapes slightly complex. As usual, the main emission band of Sm^{3+} ion is red-orange-emitting part of spectra and corresponds to ${}^4G_{5/2} \rightarrow {}^6H_{7/2}$ transition around 603 nm.

We are interested in the actual intensities of the strongest emission band, ${}^6H_{5/2} \rightarrow {}^4F_{7/2}$, of the $Y_2Mo_3O_{12}:xSm^{3+}$ samples. Thus, we plot the variation of actual intensity with the doped amount in the inset of Fig. 8(a). Since we have prepared all samples simultaneously under the same conditions (sintering procedure and preparing pellets, etc) except for the dopant concentrations, only the Sm^{3+} concentration can affect the emission characteristics. As shown in the inset, the emission intensity increases upto around 0.100 mol and then decreases, i.e. the concentration quenching is active when the Sm^{3+} concentration becomes higher than 0.150 mol in the luminescence feature. And the quenching of the emission intensity is originated from a decrease in the number of optically active Sm^{3+} ions in the samples, which means that dopant pairs and/or clusters are formed at higher concentrations of the dopant.

The observed energy levels and visible emission levels shown in Figs. 7 and 8(a) are schematically drawn in Fig. 8(b) by following the calculated energy levels [43]. From this figure, we can find that Sm^{3+} ions are excited from the ground state ${}^6H_{5/2}$ to the excited state ${}^4F_{7/2}$ with an excitation of 405 nm, then the ions at ${}^4F_{7/2}$ level relax to the ${}^4G_{5/2}$ level through the non-radiative relaxation process. Thus, the emission bands around 566 nm, 603 nm, and 649 nm arising from the transitions ${}^4G_{5/2}$ to ${}^6H_{5/2}$, ${}^6H_{7/2}$, and ${}^6H_{9/2}$, respectively, are observed.

The intensity ratio between electric and magnetic dipole transition gives a measure for the symmetry of local environment of the trivalent 4f ions [37]. Magnetic dipole transitions obey the selection rule of $\Delta J = 0$ and ± 1 , where J is the angular momentum, and electric dipole transitions obey the selection rule of $\Delta J \leq 6$ unless J or $J' = 0$ when $\Delta J = 2, 3, 6$. Thus, the transition ${}^4G_{5/2} \rightarrow {}^6H_{5/2}$ is a magnetic dipole transition because this satisfies the selection rule of $\Delta J = \pm 1$, while the transition ${}^4G_{5/2} \rightarrow {}^6H_{9/2}$ is an electric dipole transition. The transition ${}^4G_{5/2} \rightarrow {}^6H_{7/2}$ is a partly magnetic and partly forced electric dipole transition [41]. The transition ${}^4G_{5/2} \rightarrow {}^6H_{11/2}$ is not observed in this study because of its forbidden feature $\Delta J = 3$.

Consider the ratio between the intensities of the magnetic dipole transition ${}^4G_{5/2} \rightarrow {}^6H_{7/2}$ to the electric dipole transition ${}^4G_{5/2} \rightarrow {}^6H_{9/2}$, which is a measure of the local symmetry of the coordination polyhedron of the Sm^{3+} ions. Hence, the larger value of this ratio means more distortion from the inversion symmetry [37]. The obtained values are almost constant between 1.33 and 1.48, which means that the Sm^{3+} ions are embedded in samarium molybdates $[\text{Sm}_2\text{MoO}_5]$ and $[\text{Sm}_2\text{Mo}_3\text{O}_{12}]$ structures rather than in the distorted cation environment. In our previous result for $\text{CaTiO}_3:\text{Sm}^{3+}$ phosphors [37], the calculated values are from 1.40 to 1.53, which implies that the environment of Sm^{3+} ions are substituted into the host material and remain in symmetric state. Also the observed spectral widths remain similar values varying from 8.55 ~ 9.23 nm except the lower concentration samples. Therefore there is no significant structural environment change around Sm^{3+} ions with increase of the concentration, except the formation of new phases.

As mentioned in Introductory section, $\text{Y}_2\text{Mo}_3\text{O}_{12}$ is known as a NTE material having disadvantage such as hygroscopicity. From the previous discussion, we have observed a phase transition for the samples of the concentrations $x \geq 0.100$ and a concentration quenching for the samples of the higher concentrations. We can think that around 0.100 mol of Sm^{3+} -doped $\text{Y}_2\text{Mo}_3\text{O}_{12}$ is a hygroscopicity-reduced sample with highly luminescent feature. There are many studies in reducing the hygroscopicity by using the ion-substitution methods and the coating methods. As shown in this study, RE^{3+} -doped $\text{Y}_2\text{Mo}_3\text{O}_{12}$ can be a candidate material for reduced hygroscopicity as well as photonic application. We need more studies for the newly formed samarium molybdates whether these can also be host materials for photonic applications.

4. Summary

In this work, structural and optical properties of RE^{3+} -doped $\text{Y}_2\text{Mo}_3\text{O}_{12}$ material have been characterized. Sm^{3+} -doped $\text{Y}_2\text{Mo}_3\text{O}_{12}$ samples were successfully synthesized by using the two-step solid-state reaction method sintered at 300 °C and 700 °C, respectively. The synthesized samples are mostly of the orthorhombic $\text{Y}_2\text{Mo}_3\text{O}_{12}$ phase and new phases samarium molybdates $[\text{Sm}_2\text{MoO}_5]$ and $[\text{Sm}_2\text{Mo}_3\text{O}_{12}]$ appeared at higher Sm^{3+} concentration samples according to the XRD patterns. TGA results confirmed the reduction of hygroscopicity. Elemental distribution images obtained by using nano-SIMS strongly

supported the existence of Sm_2MoO_5 and $\text{Sm}_2\text{Mo}_3\text{O}_{12}$ as in XRD patterns. Raman spectra and FT-IR spectra showed phase variations, modes due to the symmetric and asymmetric vibrations of MoO_4 tetrahedron, and translational and librational vibrations of the polyhedra YO_6 and MoO_4 . XPS study showed the effect caused from Sm^{3+} -doping. Photophysical properties revealed that the appropriated amount of Sm^{3+} -doped $\text{Y}_2\text{Mo}_3\text{O}_{12}$ can possibly be an orange-red-emitting phosphor with the NUV excitation when the hygroscopicity is reduced.

Declarations

Acknowledgments

This work was supported by Korea Basic Science Institute Grants No. C39221 and PO2019052, and Busan Metropolitan City, Korea, Grant No. PO2019057.

References

1. Wu MY, Wang L, Jia Y, *et al.* Theoretical study of hydration in $\text{Y}_2\text{Mo}_3\text{O}_{12}$: Effects on structure and negative thermal expansion. *AIP Adv* 2015, **5**:027126.
2. Cheng YG, Liu XS, Song WB, *et al.* Relationship between hygroscopicity reduction and morphology evolution of $\text{Y}_2\text{Mo}_3\text{O}_{12}$ doped with $(\text{LiMg})^{3+}$. *Mater Res Bull* 2015, **65**: 273-278.
3. Cheng YG, Liu XS, Chen HJ, *et al.* In situ investigation of the surface morphology evolution of the bulk ceramic $\text{Y}_2\text{Mo}_3\text{O}_{12}$ during crystal water release. *Phys Chem Chem Phys* 2015, **17**: 10363-10368.
4. Lind C, Gates SD, Pedoussaut NM, *et al.* Novel materials through non-hydrolytic sol-gel processing: Negative thermal expansion oxides and beyond. *Mater* 2010, **3**: 2567-2587.
5. Takenaka K. Negative thermal expansion materials: technological key for control of thermal expansion. *Sci Technol Adv Mater* 2012, **13**: 013001.
6. Lind C. Two decades of negative thermal expansion research: Where do we stand? *Mater* 2012, **5**: 1125-1154.
7. Chen J, Hu L, Deng J, *et al.* Negative thermal expansion in functional materials: controllable thermal expansion by chemical modifications. *Chem Soc Rev* 2015, **44**: 3522-3567.
8. Takenaka K. Progress of research in negative thermal expansion materials: Paradigm shift in the control of thermal expansion. *Front Chem* 2018, **6**: 267.
9. Wang L, Wang F, Yuan PF, *et al.* Negative thermal expansion correlated with polyhedral movements and distortions in orthorhombic $\text{Y}_2\text{Mo}_3\text{O}_{12}$. *Mater Res Bull* 2013, **48**: 2724-2729.
10. Li ZY, Song WB, Liang EJ. Structures, phase transition, and crystal water of $\text{Fe}_{2-x}\text{Y}_x\text{Mo}_3\text{O}_{12}$. *J Phys Chem C* 2011, **115**: 17806-17811.
11. Liang E, Huo H, Wang J, *et al.* Effect of water species on the phonon modes in orthorhombic $\text{Y}_2(\text{MoO}_4)_3$ revealed by Raman spectroscopy. *J Phys Chem C* 2008, **112**: 6577-6581.

12. Ari M, Jardim PM, Marinkovic BA, *et al.* Thermal expansion of $\text{Cr}_{2x}\text{Fe}_{2-2x}\text{Mo}_3\text{O}_{12}$, $\text{Al}_{2x}\text{Fe}_{2-2x}\text{Mo}_3\text{O}_{12}$ and $\text{Al}_{2x}\text{Cr}_{2-2x}\text{Mo}_3\text{O}_{12}$ solid solutions. *J Solid State Chem* 2008, **181**: 1472-1479.
13. Miller W, Smith CW, Mackenzie DS, *et al.* Negative thermal expansion: a review. *J Mater Sci* 2009, **44**: 5441-5451.
14. Xiao XL, Cheng YZ, Peng J, *et al.* Thermal expansion properties of $\text{A}_2(\text{MO}_4)_3$ (A = Ho and Tm; M = W and Mo). *Solid State Sci* 2008, **10**: 321-325.
15. Wu MM, Peng J, Han SB, *et al.* Phase transition and negative thermal expansion properties of $\text{Sc}_{2-x}\text{Cr}_x\text{Mo}_3\text{O}_{12}$. *Ceram Int* 2012, **38**: 6525-6529.
16. Marinkovic BA, Ari M, de Avillez RR, *et al.* Correlation between AO_6 polyhedral distortion and negative thermal expansion in orthorhombic $\text{Y}_2\text{Mo}_3\text{O}_{12}$ and related materials. *Chem Mater* 2009, **21**: 2886-2894.
17. Liang EJ, Huo HL, Wang Z, *et al.* Rapid synthesis of $\text{A}_2(\text{MoO}_4)_3$ (A = Y^{3+} and La^{3+}) with a CO_2 laser. *Solid State Sci* 2009, **11**: 139-143.
18. Liu X, Cheng Y, Liang E, *et al.* Interaction of crystal water with the building block in $\text{Y}_2\text{Mo}_3\text{O}_{12}$ and the effect of Ce^{3+} doping. *Phys Chem Chem Phys* 2014, **16**: 12848-12857.
19. Liu X, Yuan B, Cheng Y, *et al.* Avoiding the invasion of H_2O into $\text{Y}_2\text{Mo}_3\text{O}_{12}$ by coating with C_3N_4 to improve negative thermal expansion properties. *Phys Chem Chem Phys* 2017, **19**: 13443-13448.
20. Dias ACT, Lima CL, Paraguassu W, *et al.* Pressure-induced crystal-amorphous transformation in $\text{Y}_2\text{Mo}_3\text{O}_{12}$. *Vib Spec* 2013, **68**: 251-256.
21. Zhou C, Zhang Q, Liu S, *et al.* Thermal mismatch strain induced disorder of $\text{Y}_2\text{Mo}_3\text{O}_{12}$ and its effect on thermal expansion of $\text{Y}_2\text{Mo}_3\text{O}_{12}/\text{Al}$ composites. *Phys Chem Chem Phys* 2017, **19**: 11778-11785.
22. Young L, Gadiant J, Lind C. High pressure behavior of chromium and yttrium molybdate ($\text{Cr}_2\text{Mo}_3\text{O}_{12}$, $\text{Y}_2\text{Mo}_3\text{O}_{12}$). *Front Chem* 2018, **6**: 478.
23. Wu MM, Xiao XL, Hu ZB, *et al.* Controllable thermal expansion and phase transition in $\text{Yb}_{2-x}\text{Cr}_x\text{Mo}_3\text{O}_{12}$. *Solid State Sci* 2009, **11**: 325–329.
24. Deng H, Zhao Z, Wang J, *et al.* Photoluminescence properties of a new orange-red emitting Sm^{3+} -doped $\text{Y}_2\text{Mo}_4\text{O}_{15}$ phosphor. *J Solid State Chem* 2015, **228**: 110-116.
25. Deng H, Xue N, Hei Z, *et al.* Close-relationship between the luminescence and structural characteristics in efficient nanophosphor $\text{Y}_2\text{Mo}_4\text{O}_{15}:\text{Eu}^{3+}$. *Opt Mater Exp* 2015, **5**: 490-496.
26. Wang Y, Liu X, Jing L, *et al.* Tunable white light and energy transfer of Dy^{3+} and Eu^{3+} doped $\text{Y}_2\text{Mo}_4\text{O}_{15}$ phosphors. *Ceram Int* 2016, **42**: 13004-13010.
27. Janulevicius M, Marmokas P, Misevicius M, *et al.* Luminescence and luminescence quenching of highly efficient $\text{Y}_2\text{Mo}_4\text{O}_{15}:\text{Eu}^{3+}$ phosphors and ceramics. *Sci Rep* 2016, **6**: 26098.
28. Mackeviciute I, Linkeviciute A, Katelnikovas A. Synthesis and optical properties of $\text{Y}_2\text{Mo}_4\text{O}_{15}$ doped by Pr^{3+} . *J Lumin* 2017, **190**: 525-530.

29. Velchuri R, Palla S, Ravi G, *et al.* Metathesis synthesis, characterization, spectral and photoactivity studies of $\text{Ln}_{2/3}\text{MoO}_4$ (Ln = La, Pr, Nd, Sm, Eu, Gd, Tb, Dy, Er and Y). *J Rare Earths* 2015, **33**: 837-845.
30. Kim YK, Lee M, Yang HS, *et al.* Optical characteristics of the rare-earth-ions-doped calcium chlorapatite phosphors prepared by using the solid-state reaction method. *Curr Appl Phys* 2016, **16**: 357-360.
31. Hong KS, Yang HS. Temperature-dependent structures and chemical bonding states of the calcium chlorapatite powders doped with rare-earth-ions. *J Korean Phys Soc* 2017, **70**: 369-374.
32. Hong KS, Yang HS. Characterization and photophysical properties of tricalcium phosphates prepared by using the solid-state reaction process. *J Korean Phys Soc* 2019, **74**: 236-240.
33. Klimesz B, Lisiecki R, Ryba-Romanowski W, Sm^{3+} -doped oxyfluorotellurite glasses – spectroscopic, luminescence and temperature sensor properties. *J Alloys Compd* 2019, **788**: 658-665.
34. Zhong Y, Deng B, Gao X, *et al.* High thermally Sm^{3+} -activated $\text{SrBi}_2\text{Ta}_2\text{O}_9$ orange-red phosphor: Preparation, characterization, and optical properties; *J Lumin* 2019, **215**: 116648.
35. Deopa N, Kumar B, Sahu MK, *et al.* Effect of Sm^{3+} ions concentration on borosilicate glasses for reddish orange luminescent device applications. *J Non-Cryst Solids* 2019, **513**: 152-158.
36. Gonzalez PA, Jahne S, Phan NTN. SIMS imaging in neurobiology and cell biology. *J Anal At Spectrom* 2019, **34**: 1355-1368.
37. Ha MG, Byeon MR, Hong TE, *et al.* Sm^{3+} -doped CaTiO_3 phosphor: Synthesis, structure, and photoluminescent properties. *Ceram Int* 2012, **38**: 1365-1370.
38. Information on <http://www.wikipedia.org> (accessed January 25, 2021).
39. Zhu Z, Hadjiev VG, Rong Y, *et al.* Interaction of organic cation with water molecule in perovskite MAPbI_3 : From dynamic orientational disorder to hydrogen bonding. *Chem Mater* 2016, **28**: 7385-7393.
40. Laufer S, Strobel S, Schleid T, *et al.* Yttrium(III) oxomolybdates(VI) as potential host materials for luminescence applications: an investigation of Eu^{3+} -doped $\text{Y}_2[\text{MoO}_4]_3$ and $\text{Y}_2[\text{MoO}_4]_2[\text{Mo}_2\text{O}_7]$. *New J Chem* 2013, **37**: 1919-1926.
41. Moulder JF, Stickle WF, Sobol PE, *et al.* *Handbook of X-ray Photoelectron Spectroscopy*. 2nd edition. Eden Prairie: Physical Electronics, 1995.
42. Watras A, Deren PJ, Pazik R. Luminescence properties and determination of optimal RE^{3+} (Sm^{3+} , Tb^{3+} and Dy^{3+}) doping levels in the KYP_2O_7 host lattice obtained by combustion synthesis. *New J Chem* 2014, **38**: 5058-5068.
43. Carnall WT, Crosswhite H, Crosswhite HM. Argonne Report ANL-78-95. Argonne: 1978.

Figures

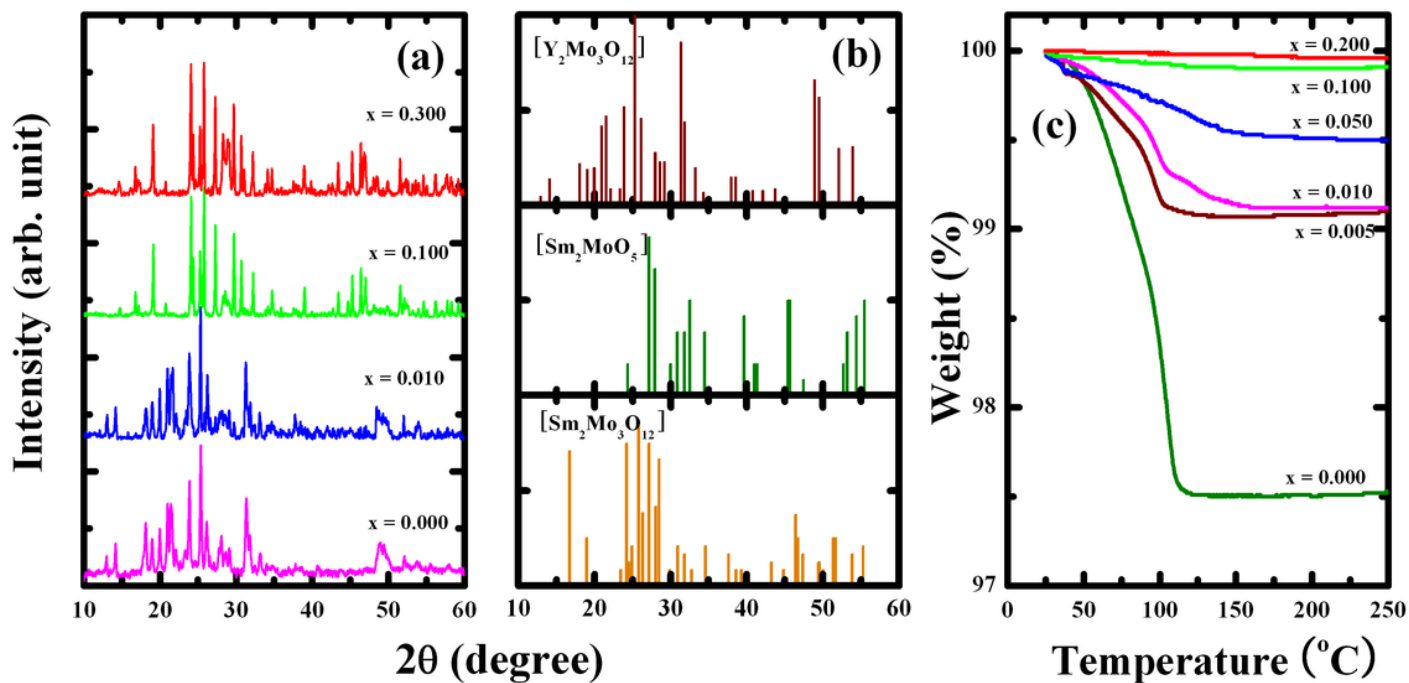


Figure 1

(a) XRD patterns of the $Y_2Mo_3O_{12}:xSm^{3+}$ powders Sm^{3+} concentrations of 0.300, 0.100, 0.010, and 0.000, from top to bottom. (b) XRD patterns of $[Y_2Mo_3O_{12}]$, $[Sm_2MoO_5]$, and $[Sm_2Mo_3O_{12}]$ phases, respectively, from JCPDS. (c) TGA analysis of the $Y_2Mo_3O_{12}:xSm^{3+}$ powders.

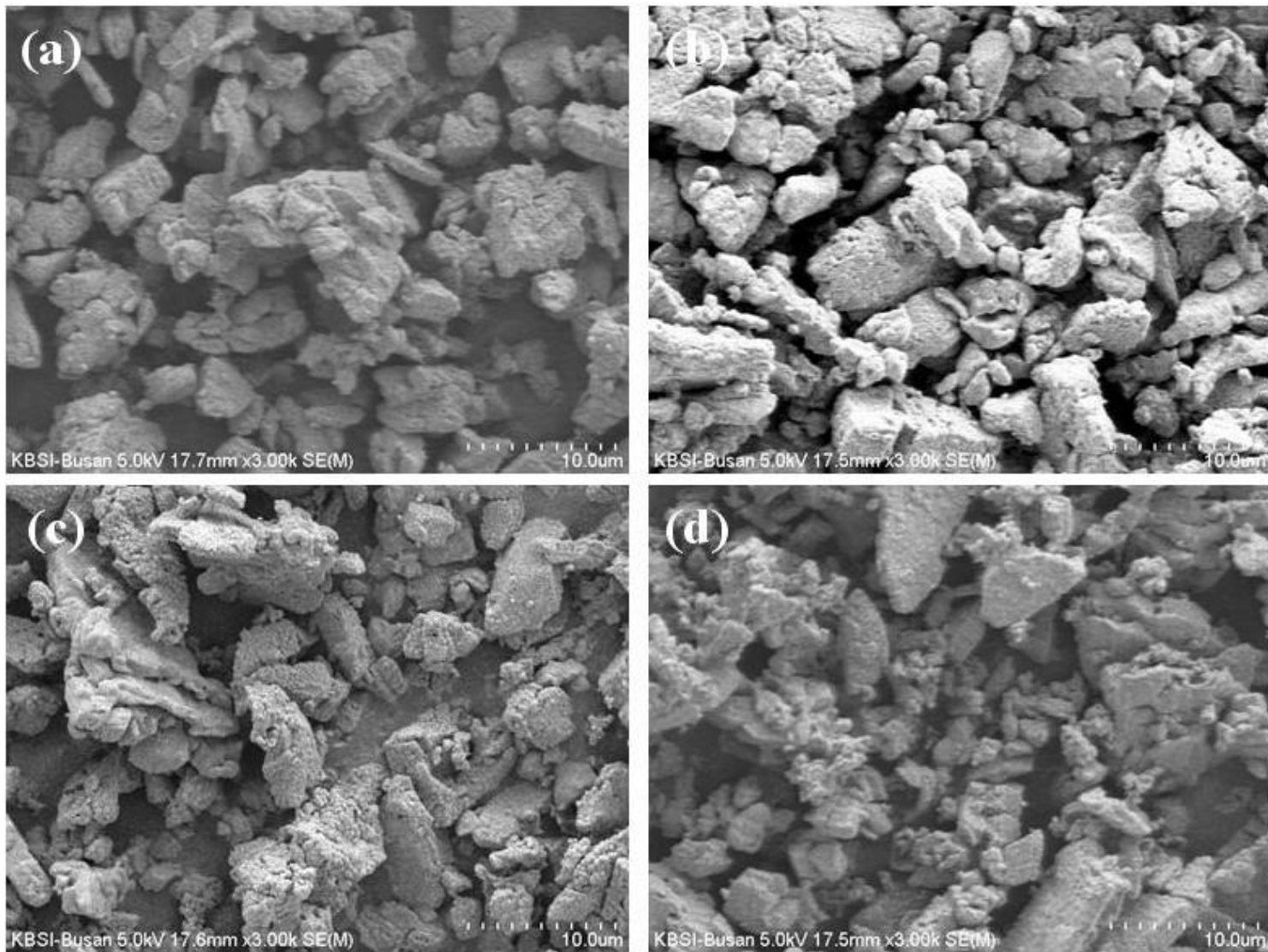


Figure 2

SEM images of the $Y_2Mo_3O_{12}:xSm^{3+}$ powders with Sm^{3+} concentrations of (a) 0.000, (b) 0.005, (c) 0.050, and (d) 0.150 mol, respectively.

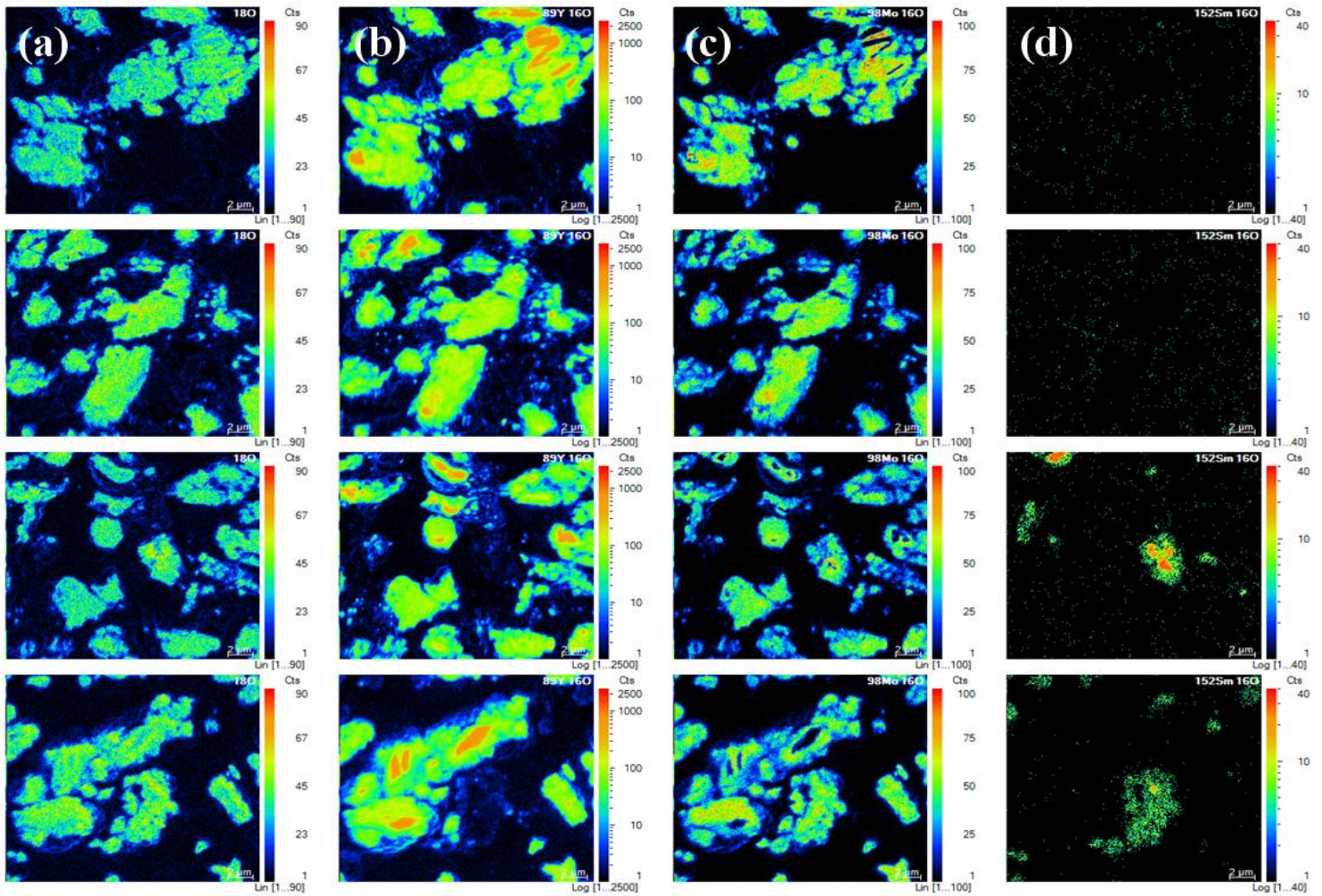


Figure 3

Elemental distribution images of (a) oxygen, (b) yttrium, (c) molybdenum, and (d) samarium in the $Y_2Mo_3O_{12}:xSm^{3+}$ powders for Sm^{3+} concentrations of 0.000, 0.005, 0.050, and 0.200 mol, respectively, from top to bottom.

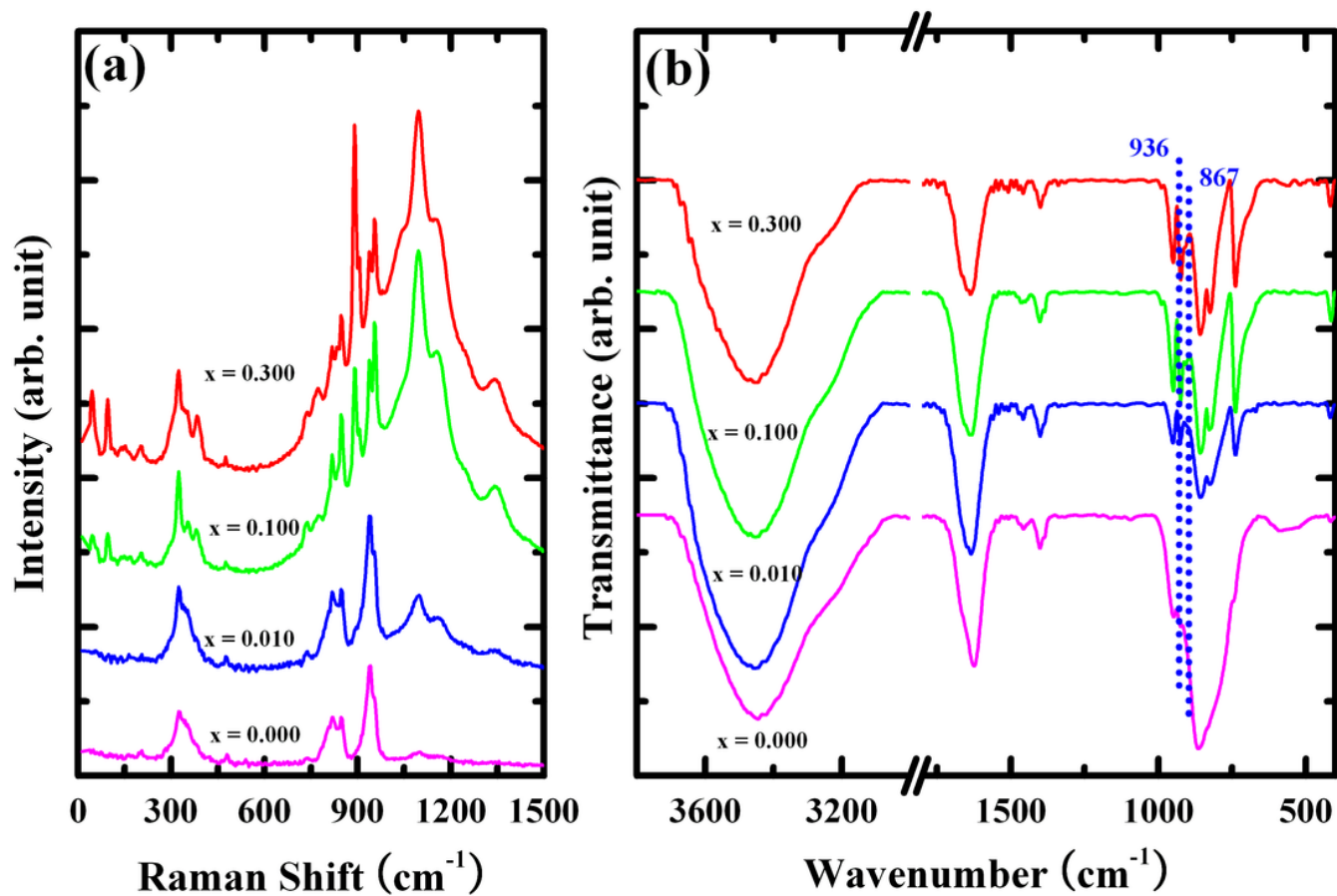


Figure 4

(a) Raman spectra and (b) FT-IR spectra of the $\text{Y}_2\text{Mo}_3\text{O}_{12}:\text{xSm}^{3+}$ samples with concentrations of 0.300, 0.150, 0.050, and 0.005 mol, respectively, from top to bottom.

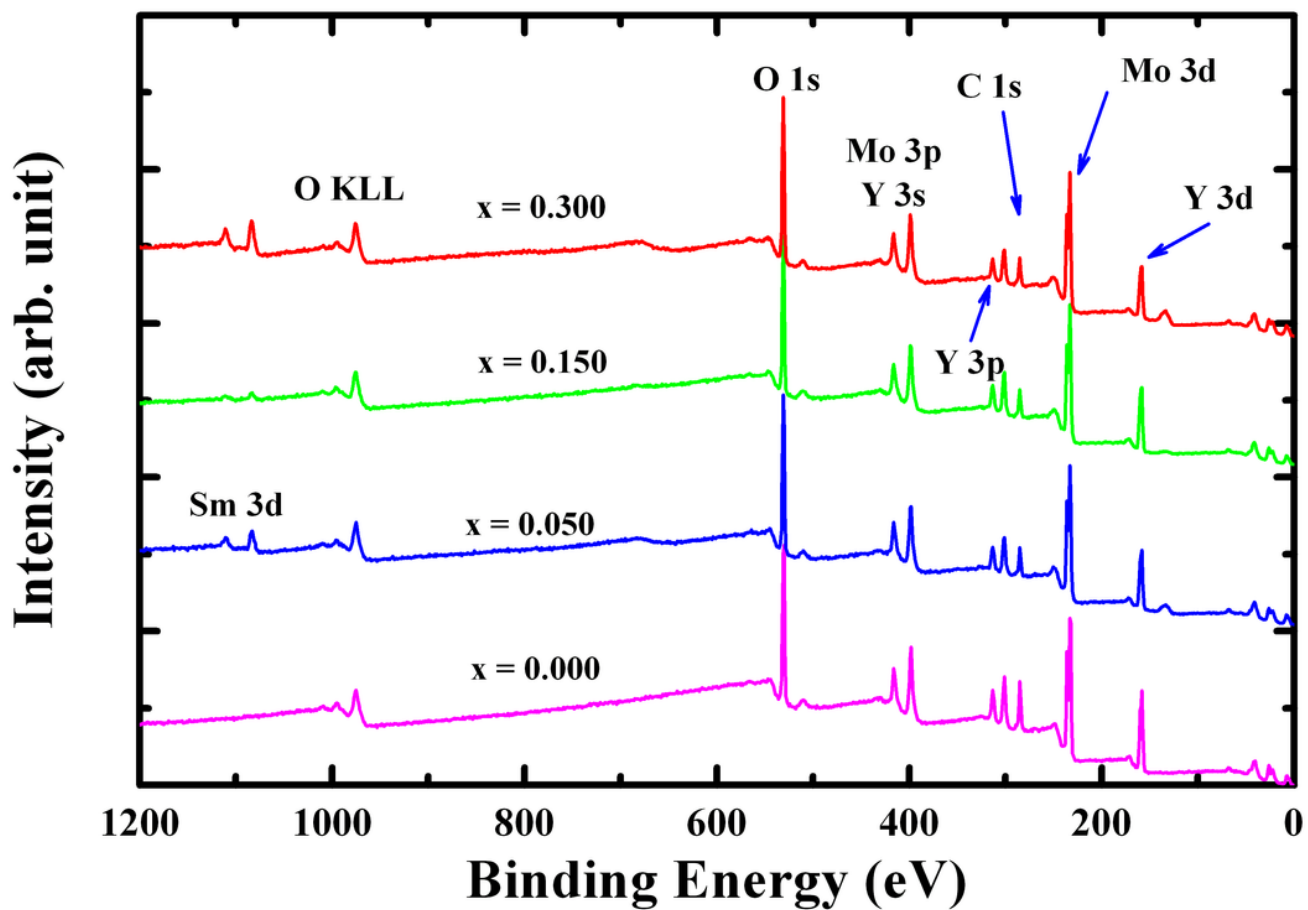


Figure 5

Wide scan XPS spectra of the $\text{Y}_2\text{Mo}_3\text{O}_{12}:\text{xSm}^{3+}$ for Sm^{3+} concentrations of 0.300, 0.150, 0.050, and 0.000 mol, from top to bottom.

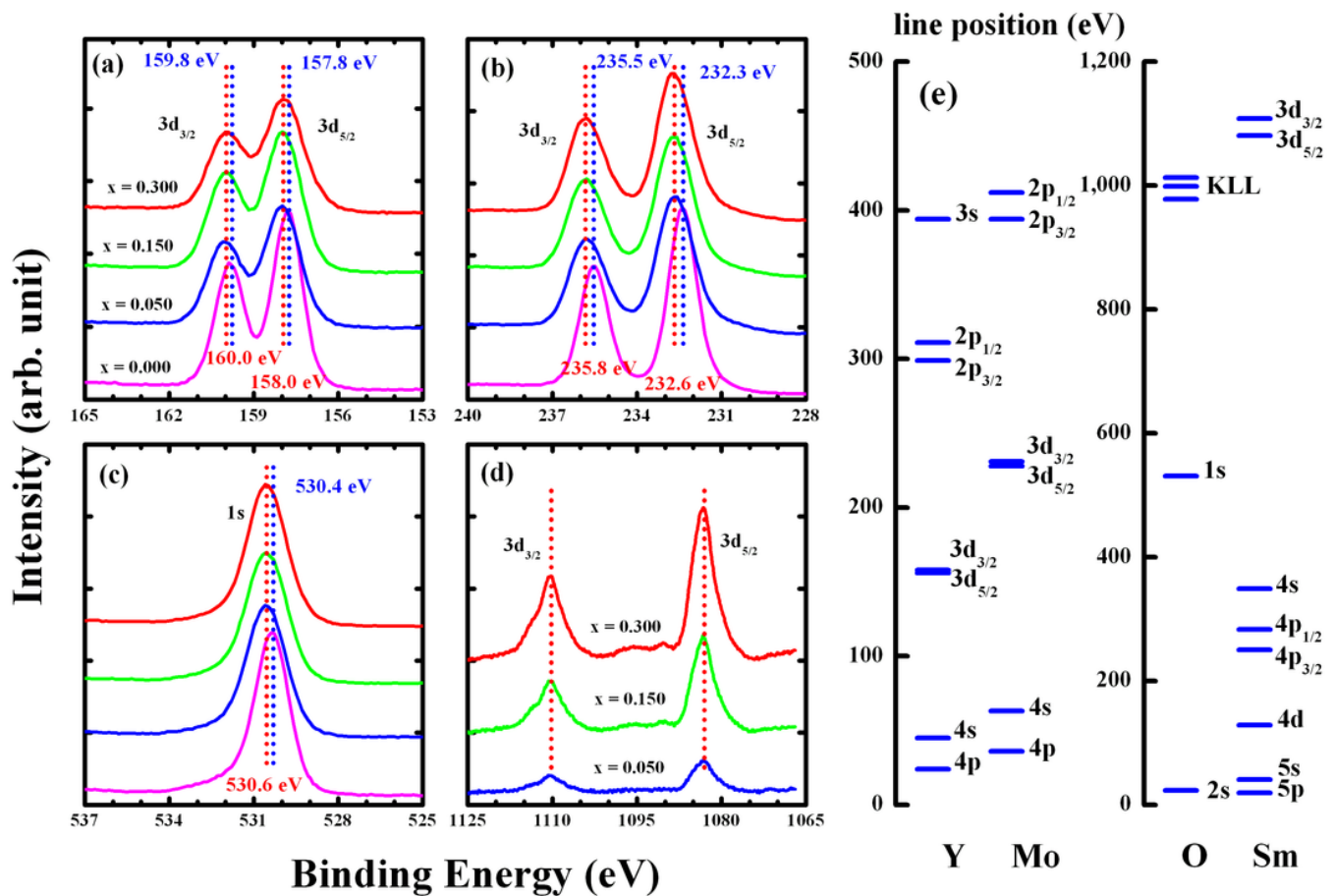


Figure 6

Narrow scan XPS spectra of (a) yttrium 3d orbitals, (b) molybdenum 3d orbitals, (c) oxygen 1s orbitals, and (d) samarium 3d orbitals in the $Y_2Mo_3O_{12}:xSm^{3+}$ samples. Concentrations of Sm^{3+} are 0.300, 0.150, 0.050, and 0.000 mol, from top to bottom, for (a)~(c). (e) Schematic photoelectron line positions of the elements Y, Mo, O, and Sm observed in Figs.5 and 6(a)-(d).

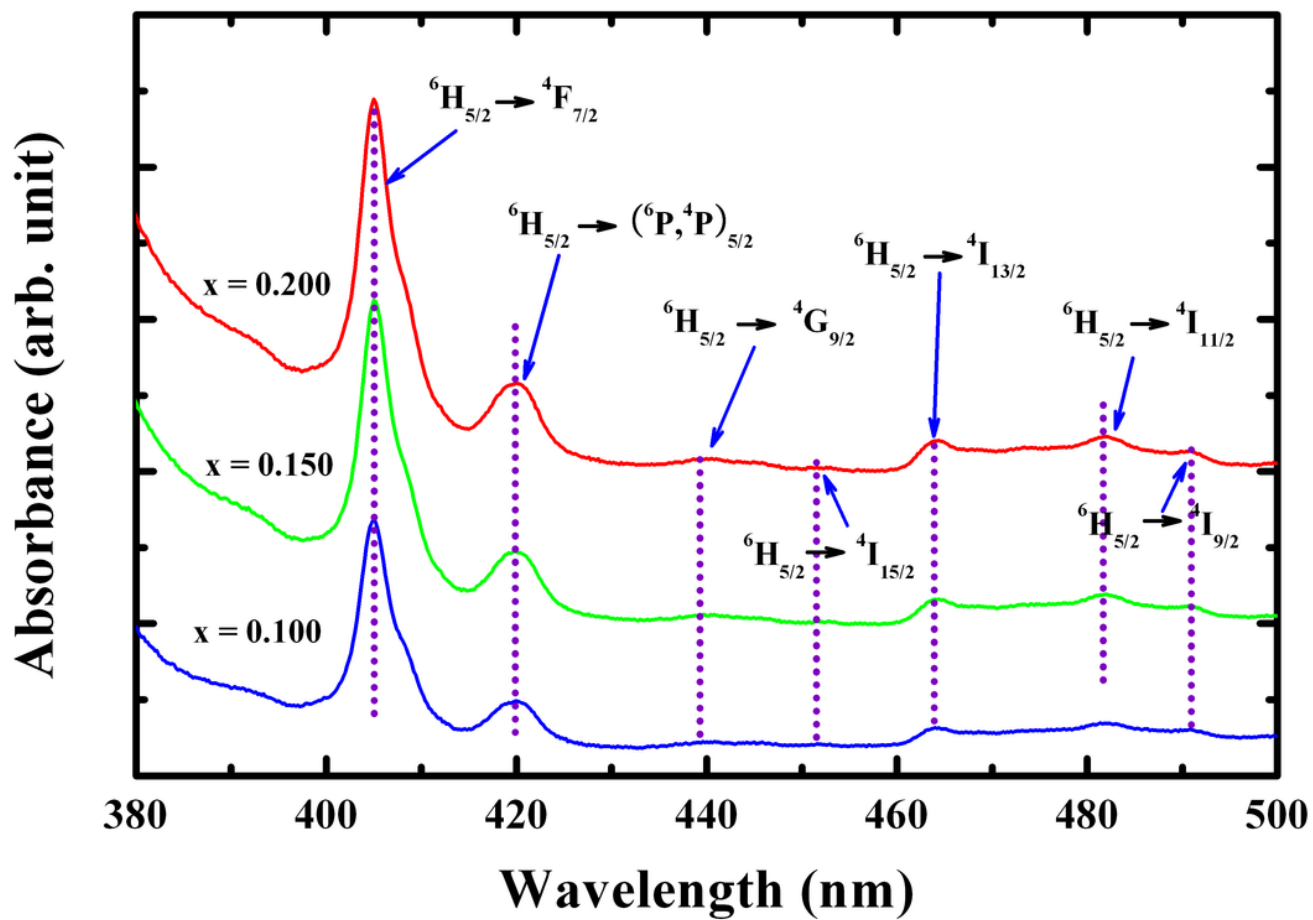


Figure 7

UV-visible absorption spectra of the Y₂Mo₃O₁₂:xSm³⁺ for concentrations of 0.200, 0.150, and 0.100 mol, from top to bottom

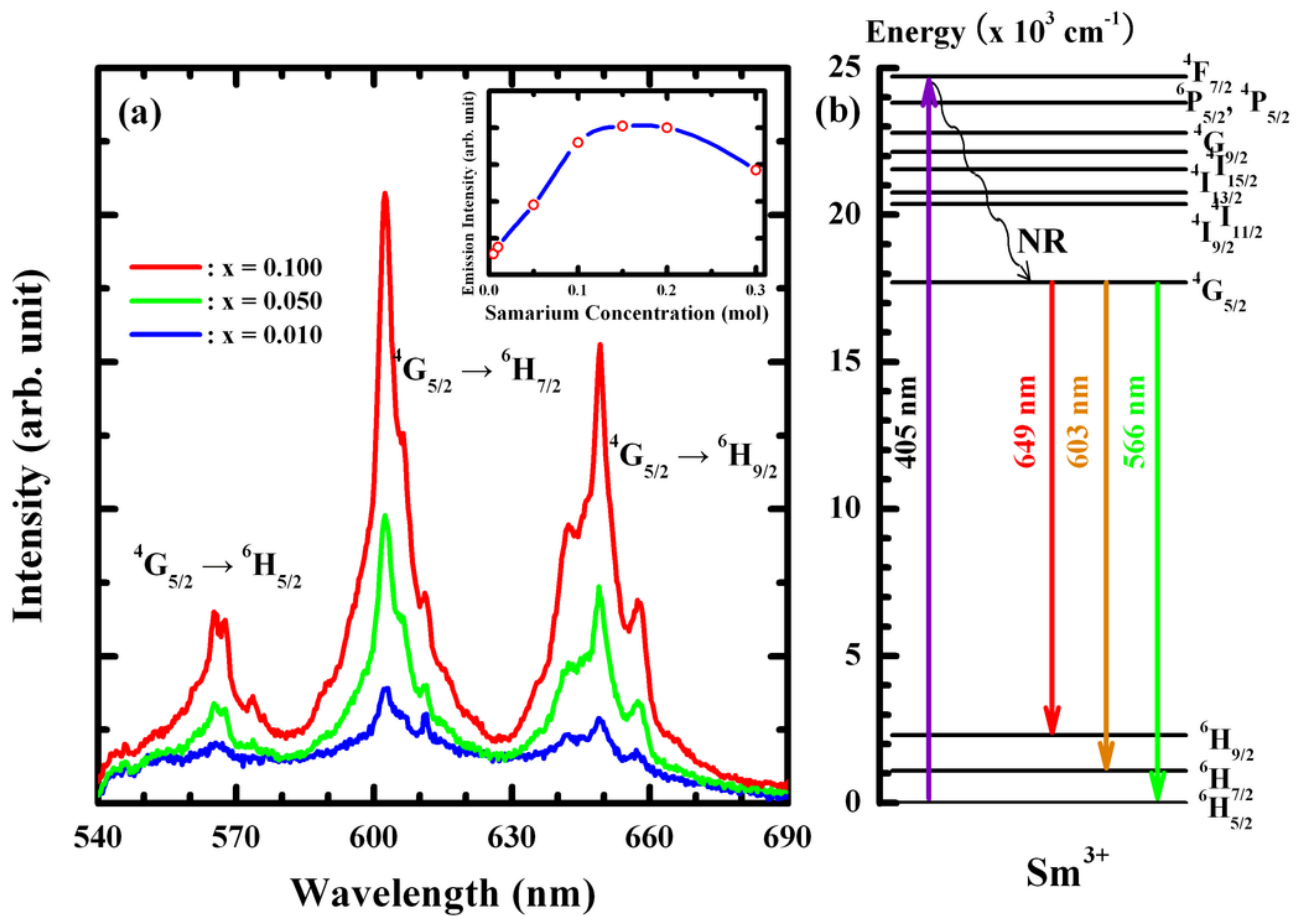


Figure 8

(a) Emission spectra of the Y₂Mo₃O₁₂:xSm³⁺ samples through the ${}^6H_{5/2} \rightarrow {}^4F_{7/2}$ excitation at 405 nm with Sm³⁺ concentrations of 0.100, 0.050, and 0.010 mol. Inset shows the concentration dependence of the emission peak ${}^4G_{5/2} \rightarrow {}^6H_{7/2}$ around 603 nm. (b) Schematic energy level diagram of the observed emission transitions in (a).